NANO LETTERS
Letter
pubs.acs.org/NanoLett

Transport Properties of Graphene Nanoroads in Boron Nitride Sheets

Jeil Jung,[†] Zhenhua Qiao,[*,†] Qian Niu,[†,‡] and Allan H. MacDonald[†]

[†]Department of Physics, The University of Texas at Austin, Austin, Texas 78712, United States
[‡]International Center for Quantum Materials, Peking University, Beijing 100871, China

Supporting Information

ABSTRACT: We demonstrate that the one-dimensional (1D) transport channels that appear in the gap when graphene nanoroads are embedded in boron nitride (BN) sheets are more robust when they are inserted at AB/BA grain boundaries. Our conclusions are based on ab initio electronic structure calculations for a variety of different crystal orientations and bonding arrangements at the BN/C interfaces. This property is related to the valley Hall conductivity present in the BN band structure and to the topologically protected kink states that appear in continuum Dirac models with position-dependent masses.

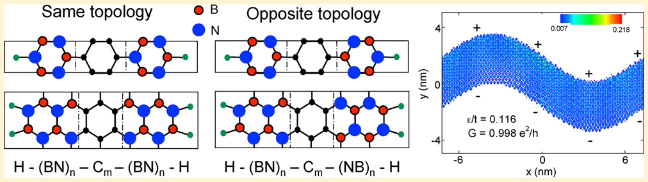

KEYWORDS: *h-boron nitride, graphene ribbon, 1D conducting state, kink state, ballistic transport*

Metallic transport channels appear at the edges, surfaces, and interfaces of two and three-dimensional (2D and 3D) bulk insulators when a bulk topological index changes value as the interface region is crossed.[1−10] This property can provide transport channels in otherwise insulating materials. The metallic states possess an internal structure related to their sense of propagation which leads to special transport properties including zero bend resistance at sharp turns in the current propagation trajectory, pseudospin memory, and suppressed backscattering.[7]

In this Letter we show that 2D hybrid structures consisting of graphene nanoroads[13] (see Figure 1) embedded in hexagonal boron nitride (BN) sheets can be an attractive host for topologically assisted one-dimensional (1D) transport channels. Our study is motivated by the observation that the π-bands of BN are similar to those of a graphene sheet, except that the honeycomb sublattices have different π-electron site energies. (The electrostatic potential is more attractive on the higher-Z N atom sites.) Because valence band states near the K and K' Brillouin-zone corners are strongly localized on N sites, whereas those elsewhere in the Brillouin-zone are divided more evenly, the bands of BN contribute with valley Hall conductivities and associated Berry curvatures of opposite signs near K and K' whose continuum model expression are given by $\Omega(\mathbf{q}) = \tau_z(3a^2\Delta t^2)/(2(\Delta^2 + 3q^2a^2t^2)^{3/2})$, where $\mathbf{q}$ is the momentum measured from a Dirac point, $\tau_z = \pm 1$ is the valley index, a is the lattice constant of the honeycomb lattice, and Δ is the band gap.[14] If the B- vs N-site potential difference was small, these Berry curvatures would be strongly concentrated near the BZ corners (see Figure 2). Indeed, in the graphene case, it is known that electronic properties in systems with sublattice staggered potentials that are weak compared to the π-bandwidth can be described using a 2D massive Dirac equation. Under these circumstances, Dirac equation continuum models are valid and predict 1D localized states along lines where the sublattice staggered potential (the Dirac equation mass) changes sign.[3,4] In the closely related bilayer[5−7] and multilayer[6] graphene cases, the sublattice staggered potentials are readily generated experimentally by applying an electric field across the layers and varied spatially by appropriately arranging external gate voltages. In the single-layer case, however, it has not been obvious how the sublattice staggered potentials could be realized, although gaps may be present with a lattice matched

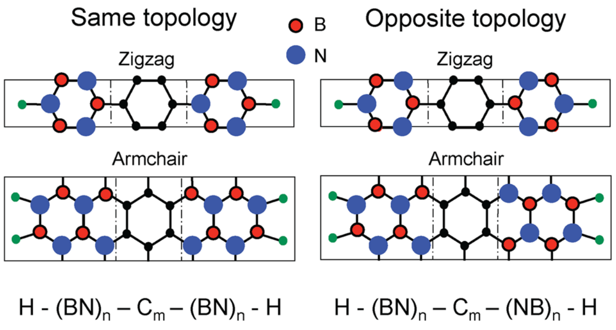

Figure 1. Schematic plot of two types of ZZ and AC BNC nanoroads. The integer n is the number of atoms in each BN partition, whereas m is the number of C atoms across the nanoroad. The outermost BN atoms are passivated with hydrogen. Left panel: The same topology arrangement in which the sign of the valley Hall effect is the same in both BN sheets. In the absence of C atoms the BN fragments can be joined seamlessly. Right panel: The opposite topology arrangement in which the sign of the valley Hall effect is opposite in the two BN sheets. In the absence of C atoms it is necessary to form a nearest-neighbor bond between atoms of the same species, either N−N and/or B−B.

Received: February 14, 2012
Revised: March 28, 2012
Published: April 23, 2012

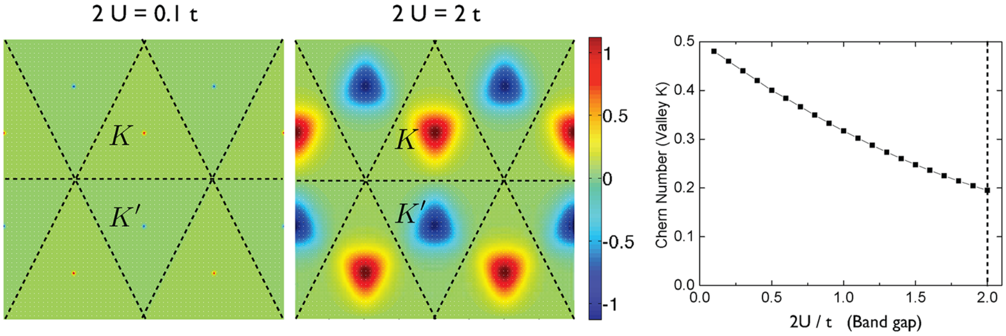

Figure 2. Berry curvatures obtained from a tight-binding model of the honeycomb lattice with different band gap sizes $\Delta = 2U$, where U is the staggering site potential. The Berry curvatures are more sharply peaked near the Brillouin zone corners K and K' when the band gap is small, and they spread out more when the gap is larger. The rightmost panel shows the deviation of the valley resolved Chern number from the ideal one-half value of the continuum model obtained integrating the Berry curvature in one equilateral triangle corresponding to one-half of the primitive cell associated to valley K given by $C_K = (2\pi)^{-1}\int_K d^2k\Omega(\mathbf{k})$. The dotted vertical line at $2U/t = 2$ indicates the valley resolved Chern number obtained for the tight-binding Hamiltonian we used to approximate the BN bands.

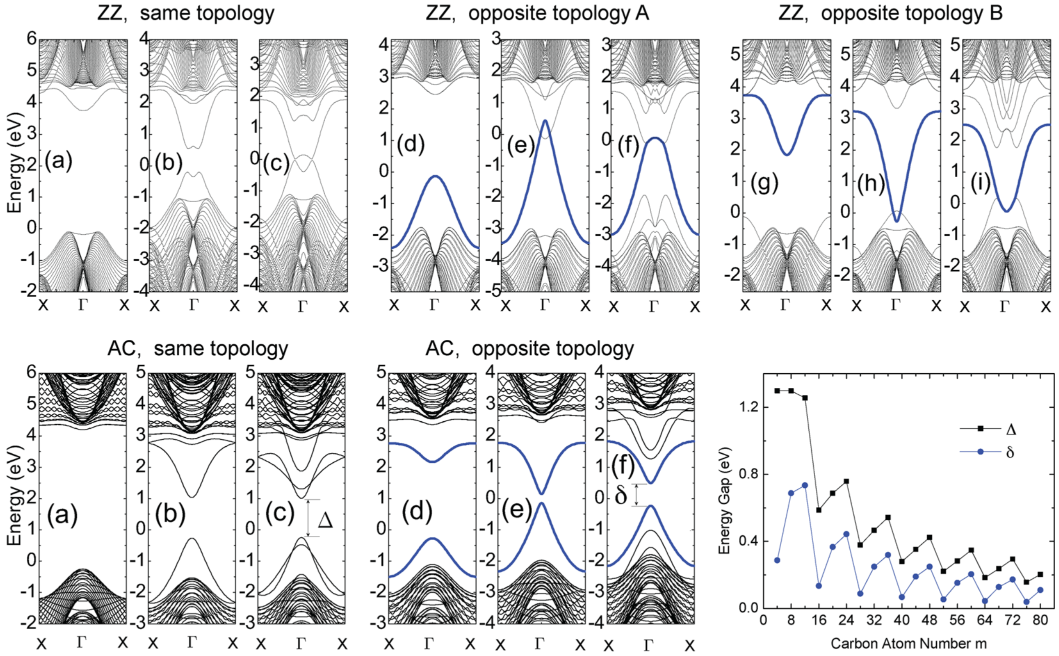

Figure 3. Upper panel: Quasi-1D band structures of ZZ graphene nanoroads of different widths embedded in hexagonal BN. The three band structures are for widths corresponding to 0, 1, and 3 complete hexagons or equivalently m = 0, 4, and 12 carbon atoms in a unit cell. The BN width number n = 40 for all cases. We consider the same topology configuration, $(BN)_n{-}C_m{-}(BN)_n$, the reversed topology configuration A, $(BN)_n{-}C_m{-}(NB)_n$, in which nitrogens bind with carbon, and reversed topology configuration B, $(NB)_n{-}C_m{-}(BN)_n$, in which borons bind with carbon. States that are peaked in the middle of the nanoroads are represented by thick blue lines. Lower panel: Band structures of AC graphene nanoroads of different widths embedded in hexagonal BN. The two band structures are for m = 0, 4, and 12 carbon atoms in a unit cell, corresponding to nanoroads that are 0, 1, and 3 hexagons wide. Same and reversed topology configurations are considered. The states that are localized in the middle of the nanoroads are again indicated by thick blue lines. As in the case of graphene nanoribbons, the gaps have an oscillatory behavior with period 12 (corresponding to 3 hexagons), embedded in a smooth envelope that follows a m^{-1} law.

BN substrate[11] or when gate potential profiles are carefully correlated with strains.[12] This work is motivated by the idea that the difference between B- and N-atom potentials in BN provides the desired staggered potential. Of course the staggered potential is not weak in the case of a BN crystal, so that expectations based on massive Dirac continuum models must be checked by ab initio electronic structure calculations.

The topological index that is inherent in BN bands can be viewed as a valley Hall effect since each valley separately supports half integer quantum Hall effects of opposite sign or at least does in the limit that the potential difference is small compared to the π-bandwidth. The properties that we discuss below are therefore closely related to the simple momentum space Berry curvature pattern in the bands of BN sheets. Hybrid BN/graphene systems of the type we study occur naturally in patched sheets containing a mixture of atomically thin graphene and BN[15] and have recently become a subject of great interest,[13,16−33] as the basis of a possible strategy for controlling graphene system band gaps. In this work we show that the properties of the transport channels formed by graphene nanoroads in BN strongly depend on the valley Hall effect of the surrounding material.

The simplest graphene nanoroad geometries have C/BN interfaces with crystallographic orientations along the zigzag

(ZZ) and armchair (AC) directions. The unit cells considered in our ab initio calculation are illustrated in Figure 1. In each case a graphene nanoribbon is flanked on the left and right by BN sheets with B and N atoms on either the same or opposite sublattices. When the two different BN fragments can be joined seamlessly preserving the crystalline B and N atom sequences upon carbon atom removal, as in the cases illustrated in the left panels of Figure 1, the BN sheets on left and right have valley Hall conductivities of the same sign, and we will say that they have the same topology. The right panels show junctions in which the BN sheets on opposite sides of the graphene nanorod have opposite valley Hall conductivities. We will refer to these configurations as having opposite topologies. When the carbon atoms are removed, joining the BN fragments would in this case require B−B or N−N bond. As shown in Figure 3, a difference in the topology of the BN sheet arrangement on the nanorod shoulders invariably leads to a qualitative change in nanorod quasi-1D band structure.

The indices n and m in Figure 3 represent respectively the number of BN and carbon atoms in the 1D unit cell. The width of the BN fragment, specified by the index n, plays a minor role in midgap state properties. We begin by discussing results for 0, 1, and 3 hexagon width ZZ nanorods presented in the upper panels of Figure 3. The 0 width cases illustrate the electronic structure of seamless BN nanoribbons with $2n = 80$ atoms of BN and therefore a width of 86 nm. The large band gap of 4 eV is comparable to that of bulk BN. There is a notable lack of particle-hole symmetry in the band structure, which is partly due to the difference between B and N site potentials mentioned previously but cannot be captured by a nearest-neighbor tight-binding model. We are mainly interested in the midgap states which emerge when a graphene nanorod is embedded in the BN sheet. As expected on the basis of the properties of pure graphene nanoribbons, we find that ZZ graphene nanorods do have strongly reduced gaps because of the presence of ZZ edge states.[35−37] There is still however a topology-sensitive feature; in the opposite topology case a midgap state appears that is peaked near the center of the nanorod, rather than at its edges, with some penetration into the BN region. This state is indicated by blue shading in Figure 3d−i. We view this state as the lattice remnant of the mass-reversal (kink) state which would appear in the opposite topology case if the staggered potential was weak and the continuum model applied. Even in the absence of carbon atoms, its appearance reduces the energy gap by approximately 2 eV. If the continuum model was accurate, there would be opposite velocity kink states associated with the K and K' valleys, and the gap would disappear entirely.

Although gaps are absent for wide nanorods in both cases, the additional kink state present for opposite topologies closes the gap already at one hexagon width in the opposite topology case. For same topology configurations, the gaps are closed because the $k_x \sim 0$ states that are most strongly localized at the edge are shifted in opposite directions by coupling to the BN shoulders.[37] For inverted topology, since the same type of atoms N or B are attached at both edges of the graphene nanorod, we see a shift of onsite energies at the edge sites in the same direction, upward for N atom bonds and downward for B atom bonds. In this case, the states closing the band gap have kink-state character and are spread widely over the C atoms of the nanorod, and with some penetration into the BN region.[7]

We now turn to AC nanorods. In ribbons this orientation does not support metallic edge states[39] and instead yields gaps which scale as the inverse ribbon width. Continuum model considerations suggest that reversed topology would lead to vanishing gaps for all widths.[6,7] The band structures in the lower panel of Figure 3 demonstrate that there are gaps in the reversed topology case but that the gaps are much smaller than those in the same topology case. The magnitude of the small avoided crossing gap between opposite velocity kink states at $k_x \sim 0$ shows the same oscillatory decline as a function of ribbon width that has been heavily studied in ribbons.[38,39] The gap reaches a value as large as 0.75 eV for AC three-hexagon nanorods. It is noteworthy that this avoided crossing is always smaller than the finite-size gap in either nanoribbons of the same width or same topology nanorods, a fact that allows the kink channels to become the main current conducting path when the Femi level of the system is adequately shifted. The same and opposite topology gaps, Δ and δ, respectively, are plotted as a function of nanorod width in the bottom right panel of Figure 3.

Zigzag graphene nanorods have bearded interface terminations when they have an odd number of carbon atoms or a non-modulo four even integer number of C atoms in the unit cell.[35,36] These interfaces are not expected to be common in experimental systems because of stability considerations. A combination of ZZ and AC fragments[34] are more abundant than bearded configurations with repeated dangling atoms. Bearded edges lead to more complicated band structures, that we discuss further in the Supporting Information, but generally preserve the tendency toward greater conduction in the opposite topology case.

To address the influence of topology on nanorod transport, we consider a two-terminal geometry with a central scattering region containing nanorods that are either straight or curved with both AC and ZZ segments (see Figure 4). In our model, the source and drain electrodes are semi-infinite ZZ graphene nanorods. The central scattering region contains 96 × 60 lattice sites, and the nanorod width is fixed at 32 carbon atoms. The BNC nanorod system is modeled using a nearest-neighbor tight-binding Hamiltonian of the form:

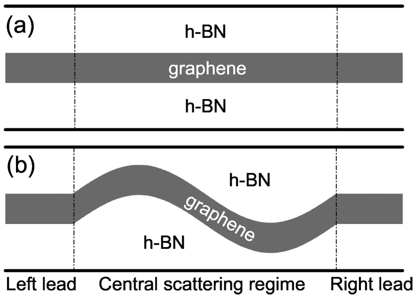

Figure 4. Schematic plot of the two-terminal BNC nanorod transport measurement that we model. (a) Straight BNC nanorods. (b) Curved BNC nanorods: the two leads are exactly the same as those in panel (a). The nanorod will support kink-like states when the two BN regions have opposite topology.

$$H = -t \sum_{\langle ij \rangle} c_i^\dagger c_j + \sum_{i \in A} U_A c_i^\dagger c_i - \sum_{i \in B} U_B c_i^\dagger c_i \tag{1}$$

where $c_i^\dagger$ (c_i) is a π-orbital creation (annihilation) operator for an electron at the site i, U_A and U_B are the BN π-orbital site energies on the A and B sublattices, and $t = 2.6$ eV is the nearest-neighbor hopping energy for both graphene and h-BN. We introduce a staggered AB sublattice potential to describe the site energy differences between B and N sublattices of h-BN, i.e., $U_B = -U_N = \lambda U_0$. Here, λ = '±' defines the crystal topology of the h-BN regions in the graphene nanoroad. U_0 measures the strength of the staggered potential, and for the purposes of this illustrative calculation, we have assumed it to be $U_0 = t$.

The temperature $T = 0$ conductance from the left to the right leads can be calculated using the multiprobe Landauer−Büttiker formula:[40]

$$G_{RL} = \frac{e^2}{h}\mathrm{Tr}[\Gamma_R G^r \Gamma_L G^a] \tag{2}$$

where $G^{r,a}$ are the retarded and advanced Green functions of the central scattering region. The quantity $\Gamma_{R/L}$ is a line width function describing the coupling between left-/right-lead and the central region and is obtained by calculating the self-energy $\sum^r_{R/L}$ of left-/right-lead using a variant transfer matrix method.[41−43]

Figure 5 plots conductance G_{RL} as a function of Fermi energy ε for the straight (ZZ-edged) and curved BNC nanoroads. In Figure 5a, the crystal topologies are the same in upper and lower h-BN regions. We observe that the conductance of the straight BNC nanoroad is quantized to be $G = 2n(e^2/h)$, where $n = 0, 1, 2, ...$ The conductance plotted here is per spin, so that the even conductance values can be attributed to the presence of ballistic states that are localized at both edges. The nanoribbon finite size effect for this nanoroad width produces a small band gap with vanishing conductance near the charge neutrality point. When the graphene nanoroad becomes curved in the central regime, disorder produces backscattering which suppresses the conductance below the quantized value.

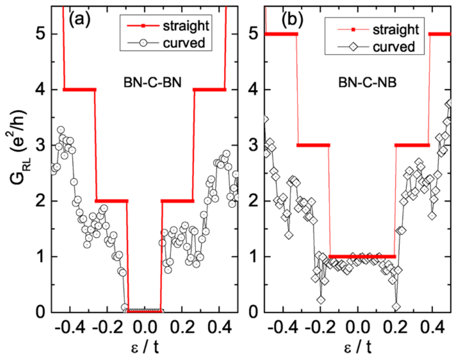

Figure 5. Conductance calculations for straight ZZ-edged and curved graphene nanoroads embedded in the h-BN as a function of the Fermi energy ε. (a) Conductance for graphene nanoroads embedded within h-BN sheets with the same topology. An insulating gap clearly arises near the charge neutrality point. (b) Graphene nanoroads embedded within h-BN sheets with different topologies. The conductance plateau near the charge neutrality region is due to a topologically supported edge state. Irregular and curved edges introduce an extremely small backscattering probability.

The case of opposite BN shoulder topologies is illustrated in Figure 5b. In this case, the conductance rule for straight BNC nanoroads is changed to $G = (2n - 1)(e^2/h)$, where $n = 1, 2, ...,$ as shown in Figure 5b. This change reflects the addition of a topologically supported kink state. For the curved reversed topology nanoribbon, the conductance does not decrease substantially in the region near the charge neutrality point where the only remaining channel is the kink state. Near the neutrality point the conductances show a surprising plateau feature with minor fluctuations that may be suppressed further by increasing the width of the graphene nanoroad. This finding strongly reflects the robustness of the crystal topology induced 1D topological conducting state against BNC nanoroad bends and is consistent with the finding of the zero bend resistance for 1D topological confinement states in gated bilayer graphene.[7]

To visualize the 1D topological conducting channel, we can evaluate the position dependence of its local density of states (LDOS) of the current originating from P^{th} lead using

$$\rho_p(\mathbf{r}, \varepsilon) = \frac{1}{2\pi}[G^r\Gamma_p G^a]_{\mathbf{rr}} \tag{3}$$

Here ε is the Fermi energy. In Figure 6, we plot the LDOS distribution of the topologically assisted conducting channel from the left lead into a snake-shaped BNC nanoroad. Our calculation shows that it is localized across the graphene atomic sites with only a small portion on the interface between h-BN and graphene. The transport calculations for the straight and curved nanoroad geometries confirm that the kink states picture remains essentially valid even when both ZZ and AC edges are simultaneously present. The almost ballistic transport is preserved in spite of irregular bonds at the graphene/BN interfaces.

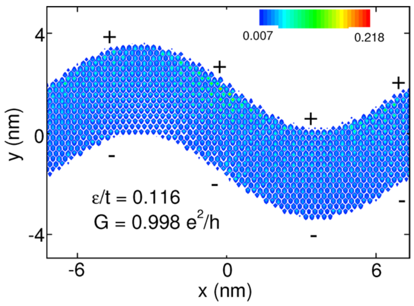

Figure 6. LDOS of a kink state in a curved carbon nanoroad embedded between opposite topology BN sheets, suggested here by the '+' and '−' signs, calculated through a nearest-neighbor tight-binding model, as discussed in the main text. The edges consist of a mixture of ZZ and AC fragments, but the disorder does not degrade transmission.

In summary, we have shown that graphene nanoroads embedded in BN sheets host kink-like transport channels when surrounded by opposite topology BN fragments. Transmission by the kink-states is topologically assisted and nearly perfect even when the graphene nanoroad is curved and has irregular edges consisting of combinations of both for ZZ and AC edges.

Calculation Details. The self-consistent ab initio calculations were carried out using the PAW-LDA parametrization of the exchange−correlation functional in a plane wave basis code, as implemented in Quantum Espresso.[44] We used 1.443 Å for the separation between neighboring B, N, and C atoms and 1.09 Å for B−H and N−H separations. These values are consistent with optimized lattice constants obtained from total energy minimization. Relaxation to obtain a final crystal geometry with atomic forces below 0.01 eV/Å had a negligible effect in modifying the interatomic distances and the band structures. For our nanoroad calculations in ribbon geometries we used 30, 1, and 1 k-points in the k_x, k_y, and k_z directions and a plane wave energy cutoff of 60 Ry. The vacuum separation distances between supercell repeated nanoribbons were set to 20 Å in both $\hat{y}$ and $\hat{z}$ directions.

■ ASSOCIATED CONTENT

Ⓢ Supporting Information

Contains a more detailed understanding of our work. This material is available free of charge via the Internet at http://pubs.acs.org/.

■ AUTHOR INFORMATION

Corresponding Author

*E-mail: zhqiao@physics.utexas.edu

Notes

The authors declare no competing financial interest.

■ ACKNOWLEDGMENTS

This work was supported by NSF (DMR 0906025), NRI-SWAN, Welch Foundation (TBF1474, F-1255), DOE (DE-FG03-02ER45958, Division of Materials Science and Engineering), and Texas Advanced Research Program. Q.N. was also supported by the MOST Project of China(2012CB921300). We gratefully acknowledge the computation resources and assistance provided by the Texas Advanced Computing Center.

■ REFERENCES

(1) Heeger, A. J.; Kivelson, S.; Schrieffer, J. R.; Su, W.-P. *Rev. Mod. Phys.* **1988**, *60*, 781.

(2) Volovik, G. E. *The Universe in a Helium Droplet*: Oxford University Press: Oxford, U.K., 2003.

(3) Semenoff, G. W.; Semenoff, V.; Zhou, F. *Phys. Rev. Lett.* **2008**, *101*, 087204.

(4) Yao, W.; Yang, S. A.; Niu, Q. *Phys. Rev. Lett.* **2009**, *102*, 096801.

(5) Martin, I.; Blanter, Ya. M.; Morpurgo, A. F. *Phys. Rev. Lett.* **2008**, *100*, 036804.

(6) Jung, J.; Zhang, F.; Qiao, Z. H.; MacDonald, A. H. *Phys. Rev. B* **2011**, *84*, 075418.

(7) Qiao, Z. H.; Jung, J.; Niu, Q.; MacDonald, A. H. *Nano Lett.* **2011**, *11* (8), 3453.

(8) Killi, M.; Wei, T.-C.; Affleck, I.; Paramekanti, A. *Phys. Rev. Lett.* **2010**, *104*, 216406.

(9) Killi, M.; Wu, S.; Paramekanti, A. *Phys. Rev. Lett.* **2011**, *107*, 086801.

(10) Wu, S.; Killi, M.; Paramekanti, A. E-print arXiv:1202.1441(2012).

(11) Giovannetti, G.; Khomyakov, P. A.; Brocks, G.; Kelly, P. J.; van den Brink, J. *Phys. Rev. B* **2007**, *76*, 073103.

(12) Low, T.; Guinea, F.; Katsnelson, M. I. *Phys. Rev. B* **2011**, *83*, 195436.

(13) (a) Singh, A. K.; Yakobson, B. I. *Nano Lett.* **2009**, *9*, 1540. (b) Bhowmick, S.; Singh, A. K.; Yakobson, B. I. *J. Phys. Chem. C* **2011**, *115*, 9889.

(14) Xiao, D.; Yao, W.; Niu, Q. *Phys. Rev. Lett.* **2007**, *99*, 236809.

(15) Ci, L.; Song, L.; Jin, C.; Jariwala, D.; Wu, D.; Li, Y.; Srivastava, A.; Wang, Z. F.; Storr, K.; Balicas, L.; Liu, F.; Ajayan, P. M. *Nat. Mater.* **2010**, *9*, 430.

(16) Rubio, A. *Nat. Mater.* **2010**, *9*, 379.

(17) Seol, G.; Guo, J. *App. Phys. Lett.* **2011**, *98*, 143107.

(18) Shinde, P. P.; Kumar, V. *Phys. Rev. B* **2011**, *84*, 125401.

(19) Pruneda, J. M. *Phys. Rev. B* **2010**, *81*, 161409(R).

(20) Li, J.; Shenoy, V. B. *Appl. Phys. Lett.* **2011**, *98*, 013105.

(21) Liu, Y.; Bhowmick, S.; Yakobson, B. I. *Nano Lett.* **2011**, *11*, 3113.

(22) Ding, Y.; Wang, Y.; Ni, J. *Appl. Phys. Lett.* **2009**, *95*, 123105.

(23) Liu, Y.; Wu, X.; Zhao, Y.; Zeng, X. C.; Yang, J. *J. Phys. Chem. C* **2011**, *115*, 9442.

(24) Fan, Y.; Zhao, M.; Zhang, X.; Wang, Z.; He, T.; Xia, H.; Liu, X. *J. Appl. Phys.* **2011**, *110*, 034314.

(25) Lam, K.-T.; Lu, Y.; Feng, Y. P.; Liang, G. *Appl. Phys. Lett.* **2011**, *98*, 022101.

(26) Berseneva, N.; Krasheninnikov, A. V.; Nieminen, R. M. *Phys. Rev. Lett.* **2011**, *107*, 035501.

(27) Ramasubramaniam, A.; Naveh, D. *Phys. Rev. B* **2011**, *84*, 075405.

(28) Obodo, K. O.; Andrew, R. C.; Chetty, N. *Phys. Rev. B* **2011**, *84*, 155308.

(29) Manna, A. K.; Pati, S. K. *J. Phys. Chem. C* **2011**, *115*, 10842.

(30) SongL. E-print arXiv:1105.1876 (2011).

(31) Modarresi, M.; Roknabadi, M. R.; Shahtahmasbi, N. *Physica E* **2011**, *43* (9), 1751.

(32) Qiu, M.; Liew, K. M. *J. Appl. Phys.* **2011**, *110*, 064319.

(33) Cao, T.; Feng, J.; Wang, E. G. *Phys. Rev. B* **2011**, *84*, 205447.

(34) Jia, X.; et al. *Science* **2009**, *323*, 1701.

(35) Fujita, M.; Wakabayashi, K.; Nakada, K.; Kusakabe, K. *J. Phys. Soc. Jpn.* **1996**, *65*, 1920.

(36) Nakada, K.; Fujita, M.; Dresselhaus, G.; Dresselhaus, M. S. *Phys. Rev. B* **1996**, *54*, 17954.

(37) Jung, J.; Pereg-Barnea, T.; MacDonald, A. H. *Phys. Rev. Lett.* **2009**, *102*, 227205.

(38) Son, Y.-W.; Cohen, M. L.; Louie, S. G. *Phys. Rev. Lett.* **2006**, *97*, 216803.

(39) Brey, L.; Fertig, H. A. *Phys. Rev. B* **2006**, *73*, 235411.

(40) Datta, S. *Electronic Transport in Mesoscopic Systems*; Cambridge University Press: Cambridge, U.K., 1995.

(41) López Sancho, M. P.; López Sancho, J. M.; Rubio, J. *J. Phys. F: Met. Phys.* **1984**, *14*, 1205.

(42) Qiao, Z. H.; Wang, J. *Nanotechnology* **2007**, *18*, 435402.

(43) Wang, J.; Guo, H. *Phys. Rev. B* **2009**, *79*, 045119.

(44) Giannozzi, P. *J. Phys. Condens. Matter* **2009**, *21*, 395502.

■ NOTE ADDED AFTER ASAP PUBLICATION

This paper was published ASAP on April 25, 2012. Reference 13(a) has been added. The revised version was posted on May 2, 2012.